



Prominent difference in the deactivation rate and mechanism of V_2O_5/TiO_2 under H_2S or SO_2 during selective catalytic reduction of NO_x with NH_3

Rongqiang Yin^{a,1}, Jianjun Chen^{a,1}, Liang Shan^a, Jianqiang Shi^{a,b}, Kun Yang^a, Hao Liu^a, Junhua Li^{a,*}

^a State Key Joint Laboratory of Environment Simulation and Pollution Control, School of Environment, Tsinghua University, Beijing 100084, PR China

^b State Key Laboratory of Clean and Efficient Coal Utilization, Key Laboratory of Coal Science and Technology, Ministry of Education, Taiyuan University of Technology, Taiyuan 030024, PR China

ARTICLE INFO

Keywords:

Nitrogen oxides
Selective catalytic reduction
Vanadium-based catalysts
Hydrogen sulfide
Sulfur dioxide

ABSTRACT

Selective catalytic reduction (SCR) over V_2O_5/TiO_2 -based catalysts is the most efficient technology to remove nitrogen oxides from stationary sources, where H_2S coexists with NO_x under variable combustion conditions. For the first time, the poisoning effect of H_2S was observed to be almost six-fold that of SO_2 . Catalyst deactivation under SO_2 was mainly caused by ammonium bisulfate while sulfates, especially polymeric sulfate, were the main contributors to H_2S poisoning. Theoretical calculations showed that the generation of sulfates was much more energetically favorable under H_2S than under SO_2 , resulting in massive deposition of sulfates and serious damage to vanadyl ($V=O$). Polymeric sulfate could inhibit the charge transfer between the occupied and unoccupied orbitals of $V=O$ and suppress NH_3 activation, thereby significantly restraining SCR activity. Furthermore, unstable sulfur species were shown to be responsible for the temporary deactivation during H_2S poisoning. This work provides crucial information for solving catalyst deactivation.

1. Introduction

Nitrogen oxides (NO_x , $x = 1, 2$) can cause acid rain, eutrophication, surface-level ozone, and haze worldwide, thus seriously endangering environment and human health [1,2]. To alleviate these detriments, selective catalytic reduction of NO_x with NH_3 (NH_3 -SCR) is used as the most efficient technology so far to remove the nitrogen oxides from both vehicles and stationary sources [1,3]. In power plants and industrial boilers, V_2O_5/TiO_2 -based catalysts are widely used because of their relatively high activity and selectivity [4,5]. However, despite their great performance in the starting stage, the vanadium-based catalysts can be poisoned by sulfur, alkali, and heavy metal [5,6]. Therefore, it is necessary to explore the poisoning mechanism to upgrade SCR catalysts [2].

Due to the sulfur deactivation of vanadium-based catalysts, it is quite difficult to realize the long-term stable operation of the SCR reactor at low temperatures ($< 300\text{ }^\circ\text{C}$) [7,8]. Hydrogen sulfide and other sulfur components are typical impurities in various fuels, including kerosene, natural gas, coal gas, and bio-gas [9–11]. Under incomplete combustion,

part of the sulfur is converted to sulfur dioxide, another part exists in the flue gas as H_2S [11–13], and burning sulfur-containing coal in low air-to-fuel ratio can also result in the formation of H_2S [14,15]. Hence, SO_2 and H_2S coupled with NO_x coexist in the flue gas of various industrial boilers, such as glass furnaces ($< 200\text{ ppm}$) [15]. However, despite previous reports on the poisoning effect of SO_2 , to our best knowledge, no report is available regarding the poisoning mechanism of H_2S on SCR catalysts at molecule-level [1,16].

Under SO_2 poisoning, the deactivation of vanadium-based catalysts was mainly caused by the physical coverage resulting from SO_2 -derivative ammonium bisulfate [1,8], while some other SCR catalysts are poisoned due to the formation of metal sulfates and the destruction of active sites [17,18]. When applied for H_2S selective oxidation, V_2O_5/TiO_2 -based catalysts may be deactivated by the cover of elemental sulfur at low temperatures ($< 180\text{ }^\circ\text{C}$) and low O_2 concentrations (O_2/H_2S mole ratio < 1) [19,20]. As for SCR, in the flue gas of typical industrial boilers ($> 180\text{ }^\circ\text{C}$, $O_2/H_2S > 200$), most of H_2S is converted to SO_2 , and a part deposits as sulfates on the catalysts [21]. Nevertheless, some uncertainties need to be clarified: (i) whether the sulfur species

* Corresponding author.

E-mail address: lijunhua@tsinghua.edu.cn (J. Li).

¹ R. Yin and J. Chen contributed equally.

generated from H₂S are the same as those generated from SO₂; (ii) whether the species damage the structure of V₂O₅/TiO₂-based catalysts; and (iii) how the sulfur species impact SCR reaction. Hence, revealing the H₂S poisoning mechanisms is fundamentally important for solving the deactivation and designing sulfur-resistant catalysts.

In this work, we comparatively investigated the poisoning effect of H₂S or SO₂ on vanadium-based catalysts. As SCR reactors are usually operated at 200–300 °C at the glasswork and coking plant [11], the catalysts with ~3 wt% V₂O₅ were synthesized to ensure the high activity, and the resistance to H₂S or SO₂ was estimated at 250 °C. The results indicated that the activity decline rate under H₂S was approximately six-fold that under SO₂. To figure out why the catalysts were destroyed so fast by H₂S, systematic characterizations, including both ex situ and in situ measurements, and density functional theory (DFT) calculations, were conducted to analyze the fresh, H₂S-poisoned, and SO₂-poisoned catalysts. Finally, the inhibition mechanism of SCR reaction was explored and several poisoning routes were proposed at molecular level.

2. Experimental methods

2.1. Catalysts preparation

3%V₂O₅/TiO₂ (VTi-O), 3%V₂O₅-3%WO₃/TiO₂ (VWTi-O) and 3%V₂O₅-3%MoO₃/TiO₂ (VMOti-O) were prepared by impregnation. Typically, 193 mg NH₄VO₃ and 416 mg H₂C₂O₄·H₂O were dissolved with 5 mL deionized water in a 250 mL beaker. For, VWTi-O and VMOti-O, 160 mg H₂₈N₆O₄₁W₁₂ (Ammonium metatungstate) or 184 mg H₂₄Mo₇N₆O₂₄·4 H₂O (Ammonium heptamolybdate) was dissolved. Then, 5.00 g TiO₂ (Aladdin, T104943) was added. With stirring, the suspension was heated with water bath at 50 °C until the suspension transformed into a solid-state yellow cake. After vacuum drying overnight at 50 °C, the cake was calcined at 450 °C for 5 h (5 °C/min).

To reduce the influence of intrinsic sulfur in commercial TiO₂ (Aladdin, T104943) on the analysis of sulfur-deposition during H₂S or SO₂ inhibitory effect tests, the commercial TiO₂ was calcined at 700 °C for 2 h (5 °C/min). After this pretreatment, the sulfur content (calculated in form of SO₃) reduced from 2.1% to 0.3%, which was detected by X-ray fluorescence (Table S1). The pretreated TiO₂ with low sulfur content was denoted as TiO₂-L. Then, 3%V₂O₅/TiO₂-L, 3%V₂O₅-3%WO₃/TiO₂-L, 3%V₂O₅-3%MoO₃/TiO₂-L (denoted as VTi, VWTi, VMOti) were synthesized by the same method as mentioned above except the commercial TiO₂ was replaced by TiO₂-L. The poisoned samples were obtained by vapor-phase treatment. 100 mg 40–60 mesh VTi catalyst was loaded in the same reactor as the activity test below and the reactor was heated to 250 °C (10 °C/min) in air. Then, the catalyst was treated for 5 h in a 400 mL/min gas mixture containing 1000 ppm H₂S (or SO₂), 10% O₂, 5% H₂O, and N₂ (balance gas). After cutting off the gas mixture, the reactor was cooled down to 50 °C. The catalyst pretreated by H₂S or SO₂ was denoted as VTi-HS or VTi-S.

2.2. Activity test

Typically, 100 mg 40–60 mesh catalyst was loaded in an L-type quartz tube with 400 mL/min gas mixture, 240,000 mL·g⁻¹·h⁻¹ gas hourly space velocity (GHSV), containing 500 ppm NO_x, 500 ppm NH₃, 10% O₂, 5% H₂O, and N₂ (balance gas). The ramping rate was 10 °C/min and the hold time was 20 min at each temperature point. The inhibitory effect of H₂S was evaluated with 1000 ppm H₂S to amplify the phenomenon and represent the deactivation in the long-term operation. Accordingly, the inhibitory effect of SO₂ was evaluated with 1000 ppm SO₂ for better comparison. The concentrations of NO_x, NH₃, N₂O, and SO₂ were monitored by an Infrared spectrometer (Gaset DX-4000, Finland). The concentration of H₂S was detected by gas chromatograph (FULI GC9790 Plus, China) with a flame photometric detector (FPD). NO_x conversion, N₂ selectivity, and SO₂ yield ratio were computed using the following equations.

$$NO_x \text{ conversion} = \frac{C_{NO_x}^{in} - C_{NO_x}^{out}}{C_{NO_x}^{in}} \times 100\% \quad (1)$$

$$N_2 \text{ selectivity} = \left[1 - \frac{2C_{N_2O}^{out}}{C_{NO_x}^{in} + C_{NH_3}^{in} - C_{NO_x}^{out} - C_{NH_3}^{out}} \right] \times 100\% \quad (2)$$

$$SO_2 \text{ yield ratio} = \frac{C_{SO_2}^{out}}{C_{H_2S}^{in}} \times 100\% \quad (3)$$

2.3. Characterization

The physical-chemical property of the catalysts was evaluated by inductively coupled plasma-optical emission spectroscopy (ICP-OES), X-ray powder diffraction patterns (XRD), Brunauer-Emmett-Teller-Barrett-Joyner-Halenda (BET-BJH), X-ray photoelectron spectroscopy (XPS), electron paramagnetic resonance (EPR), ultraviolet-visible diffuse reflection spectroscopy (UV-Vis DRS). The details were stated in the [Supporting Information](#).

The elemental analysis of nitrogen was conducted on a LECO ONH863 instrument (USA). Fourier Transform Infrared Spectroscopy (FTIR) test was conducted on a Nicolet iS 50 (Thermo Fisher, USA) spectrometer. The chemical bond structure of vanadium species on VTi, VTi-HS, and VTi-S was obtained on an ex situ Raman spectrometer (Horiba LaRAM HR Evolution, Horiba Jobin Yvon, France). In each test, the sample was heated to 250 °C (10 °C/min) in 50 mL/min 10% O₂/N₂ and held for 10 min. Then, the Raman spectra were obtained with a 532 nm laser. In situ Diffuse Reflectance Infrared Fourier Transform Spectroscopy (In situ DRIFTS) test was conducted on a Nicolet iS 50 (Thermo Fisher, USA) spectrometer. For H₂S (or SO₂) DRIFTS, the VTi catalyst was pretreated in 50 mL/min 10% O₂/N₂ at 400 °C for 15 min. After cooling down to 250 °C and holding for 30 min, the background was recorded. Then, spectra series I (60 min) was collected in a gas mixture consisting of 5000 ppm H₂S (or SO₂), 10% O₂, and N₂ (balance gas), which was followed by spectra series II (200 min) was collected in 10% O₂/N₂. For NH₃ DRIFTS and SCR DRIFTS, the details can be found in [Supporting Information](#).

Quasi in situ X-ray photoelectron spectroscopy (Quasi in situ XPS) was conducted on an Escalab 250Xi (Thermo Fisher, USA) with Al Ka (hν=1486.6 eV) radiation under 30 eV pass energy, scanning 10 times for V 2p, O 1s, Ti 2p, and 50 times for S 2p. The calibration was carried out according to C 1s (284.8 eV). For each test, the VTi catalyst was pretreated in 50 mL/min 10% O₂/N₂ at 250 °C for 30 min. Then, the sample was treated in a gas mixture consisting of 5000 ppm H₂S (or SO₂), 10% O₂, and N₂ (balance gas) for 30 min at 250 °C, which was followed by vacuumizing and spectra collection. Besides, the XPS spectrum of fresh VTi was collected after the reactor was vacuumized without sulfur pretreatment. The decomposition of sulfate in the catalysts: 100 mg 40–60 mesh catalyst was loaded in the same reactor as the activity test above, and the reactor was heated to 250 °C (10 °C/min) in 10% O₂/N₂. Then, the reactor was heated to 600 °C (10 °C/min) in 100 mL/min N₂.

2.4. DFT + U simulation

Spin-polarized calculations were conducted by Vienna Ab initio Simulation Package (VASP, version 5.4.4). The model of VTi was built on anatase TiO₂ (001) with a V₂O₅ molecule, representing as V₂O₇ cluster (Fig. S1), due to the polymeric vanadyl species are regarded as the main active sites of SCR [6,22,23]. The U_{eff} (U–J) of V and Ti were set at 3 and 4.5 eV, respectively. 0.05 eV/Å of maximum atomic force was used for the geometrical optimization of intermediate states and transition states. The dimer method was employed to search the transition states during the dehydrogenation of NH₃. Further, the energy of transition states was calibrated by frequency calculation and the

temperature was set at 250 °C by VASPKIT (version 1.2.5). Related details can be found in [Supporting Information](#).

3. Results and discussion

3.1. Inhibition on SCR performance

First, we tested the poisoning effect of H₂S on the catalysts prepared by commercial TiO₂ ([Fig. S2](#)), including 3%V₂O₅/TiO₂ (VTi-O), 3%V₂O₅-3%WO₃/TiO₂ (VWTi-O) and 3%V₂O₅-3%MoO₃/TiO₂ (VMTi-O), all of which contained ~3% V₂O₅ ([Table S2](#)). In the presence of H₂S, all the three catalysts showed inferior activity below 300 °C, in contrast to no activity decline above 350 °C ([Fig. S2](#)). For better understanding the deposition of sulfur species, the reagent TiO₂ was pretreated at 700 °C to reduce the original sulfur species (details were stated in [Section 2.1](#)) and the catalysts based on the pretreated TiO₂ were denoted as VTi, VWTi, and VMTi, respectively. These three catalysts also showed inferior activity under H₂S below 300 °C, among which VTi showed the best resistance ([Fig. S2](#)). SO₂ was reported to be oxidized by surface WO_x sites [16], so we proposed that H₂S could also be oxidized by the surface tungsten and molybdenum species, causing more serious deactivation of VWTi and VMTi than VTi. To exclude the effects of W or Mo and simplify investigation, we took VTi as an example to study the H₂S poisoning mechanism in the following experiments.

For a comparative study, the deactivation behavior of VTi under H₂S or SO₂ was tested separately at 250 °C ([Fig. 1a](#)). After injecting SO₂, the NO_x conversion over VTi showed a rapid decline from 69% to 40% in 300 min, similar to the previous reports [1,24]. Strikingly, after introducing H₂S, the activity of VTi decreased from 69% to 40% in only 53 min, with the decline rate being six-fold that under SO₂ poisoning. Furthermore, NO_x conversion continued to decline until 3% in 300 min, i.e., the activity of VTi was almost fully destroyed. After excluding H₂S, the SCR activity of VTi increased from 3% to 19% in 120 min and remained almost constant in the following 120 min. Noteworthily, the final stable activity after H₂S poisoning (19%) was much lower than that under SO₂ (40%), and such a serious poisoning effect of H₂S may cause a huge difficulty in application.

Unlike the deactivation under SO₂ exposure, there was a recovery stage of activity after stopping H₂S injection, indicating a difference in the poisoning mechanism under H₂S. Meanwhile, this phenomenon implied that both stable and unstable factors impacted the activity of VTi during H₂S poisoning. The unstable factors influencing NO_x conversion would be discussed in [Section 3.5](#). Considering the stable factors may be more significant in the long term, we first tried to figure out why the final activity was much lower under H₂S than under SO₂.

Herein, we pretreated the catalyst under different gas compositions

containing H₂S at 250 °C for 300 min ([Fig. S3](#)). Then, after reaction in SCR condition (NO_x, NH₃, and O₂) for 120 min, the stable NO_x conversion over the pretreated catalysts was summarized in [Fig. 1b](#). Apparently, under the three conditions containing “H₂S+O₂”, the deactivation extent was approximately the same, where the extra deactivation under “NO_x+NH₃+H₂S+O₂” may be caused by the cover effect of ammonium bisulfate [1,24]. In contrast, no obvious deactivation occurred after “H₂S” pretreatment. These results indicated that “H₂S+O₂” was probably the key inducer of H₂S poisoning, and the catalyst pretreated under “H₂S+O₂” was denoted as VTi-HS in the following investigation. Accordingly, the final NO_x conversion over the catalysts pretreated by SO₂ was also summarized in [Fig. 1b](#). The “NO_x+NH₃+SO₂+O₂” gas composition was found to cause much more serious deactivation than “SO₂+O₂” or “SO₂”. This result suggested that “NO_x+NH₃+SO₂+O₂” was the main reason for SO₂ poisoning, where SO₂ was oxidized to SO₃ and then reacted with H₂O and NH₃ to form NH₄HSO₄ [1,24].

Whether “H₂S+O₂” is the key inducer of H₂S poisoning was further verified through a set of characterizations. Apart from VTi-HS, the samples pretreated with “SO₂+O₂” (VTi-S), “NO_x+NH₃+H₂S+O₂” (VTi-HS-N) and “NO_x+NH₃+SO₂+O₂” (VTi-S-N) were also analyzed. Temperature programmed decomposition was conducted to analyze the deposited species ([Fig. 2a](#)). In the case of both VTi-HS-N and VTi-S-N, the peak value of SO₂ and NH₃ emission appeared at ~400 °C and ~350 °C, which were close to the decomposition temperatures of ammonium bisulfate deposited on V₂O₅/TiO₂ catalysts [25], suggesting the existence of ammonium bisulfate on these two catalysts. However, the ratio of SO₂/NH₃ emitted from VTi-HS-N was obviously higher than that of VTi-S-N, as confirmed by the elemental analysis ([Fig. 2b](#)) and XPS results ([Fig. S4](#)). These results suggested that the species deposited on VTi-HS-N and VTi-S-N were not fully identical. Besides, as shown in [Fig. 2c](#), the sulfur species deposited on VTi-HS and VTi-S were also decomposed around 400 °C, implying the co-existence of sulfates on the surface of VTi-HS-N and VTi-S-N.

Moreover, FTIR results ([Fig. 2d](#)) revealed the accumulation of both ammonium bisulfate (1395, 1185, 1127, 1067, and 969 cm⁻¹) [25,26] and surface sulfates (1351, 1325, 1185, 1127, and 969 cm⁻¹) [27,28] on VTi-HS-N and VTi-S-N. This may be attributed to: (i) direct generation of sulfates from the oxidation of H₂S and SO₂, and (ii) the decomposition onset of ammonium bisulfate at 250 °C to generate NH₃ and sulfates [25]. Besides, the ratio of peak intensity at 1127/1395 cm⁻¹ was higher in VTi-HS-N than in VTi-S-N, indicating the ratio of sulfates/ABS on VTi-HS-N was higher than VTi-S-N, agreeing with the above elemental analysis. Notably, VTi-HS also showed obviously strong peaks related to sulfates, while VTi-S displayed much weaker peaks ([Fig. 2d](#)). Based on these characterizations and above activity analysis, the sulfates on VTi-HS-N can be concluded to be mainly generated directly from the

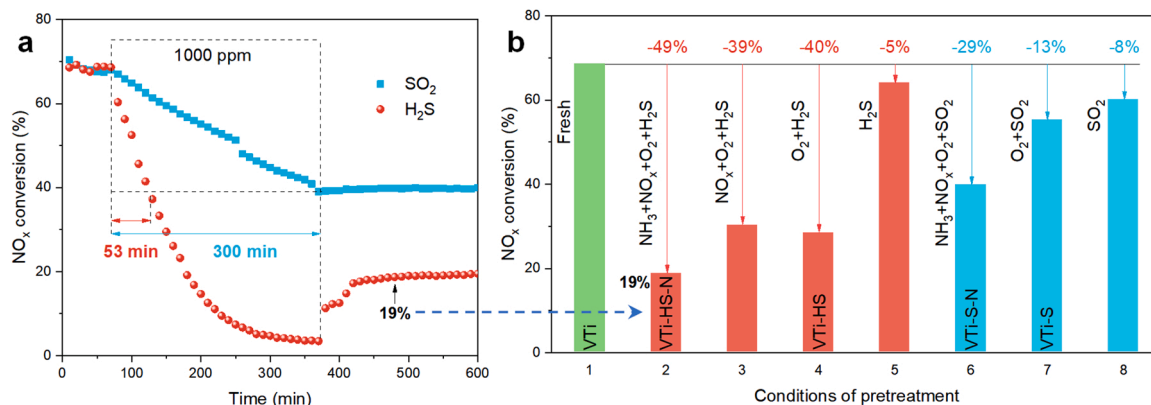


Fig. 1. (a) Time-varying NO_x conversion over VTi at 250 °C when H₂S or SO₂ was introduced. (b) The stable NO_x conversion over VTi after pretreatment with different gas compositions. Pretreatment conditions: 240,000 mL·g⁻¹·h⁻¹ GHVS, 500 ppm NO_x (when used), 500 ppm NH₃ (when used), 1000 ppm H₂S or SO₂ (when used), 10% O₂, 5% H₂O, and N₂ (balance gas). Reaction conditions: 240,000 mL·g⁻¹·h⁻¹ GHVS, 500 ppm NO_x, 500 ppm NH₃, 10% O₂, 5% H₂O, and N₂ (balance gas).

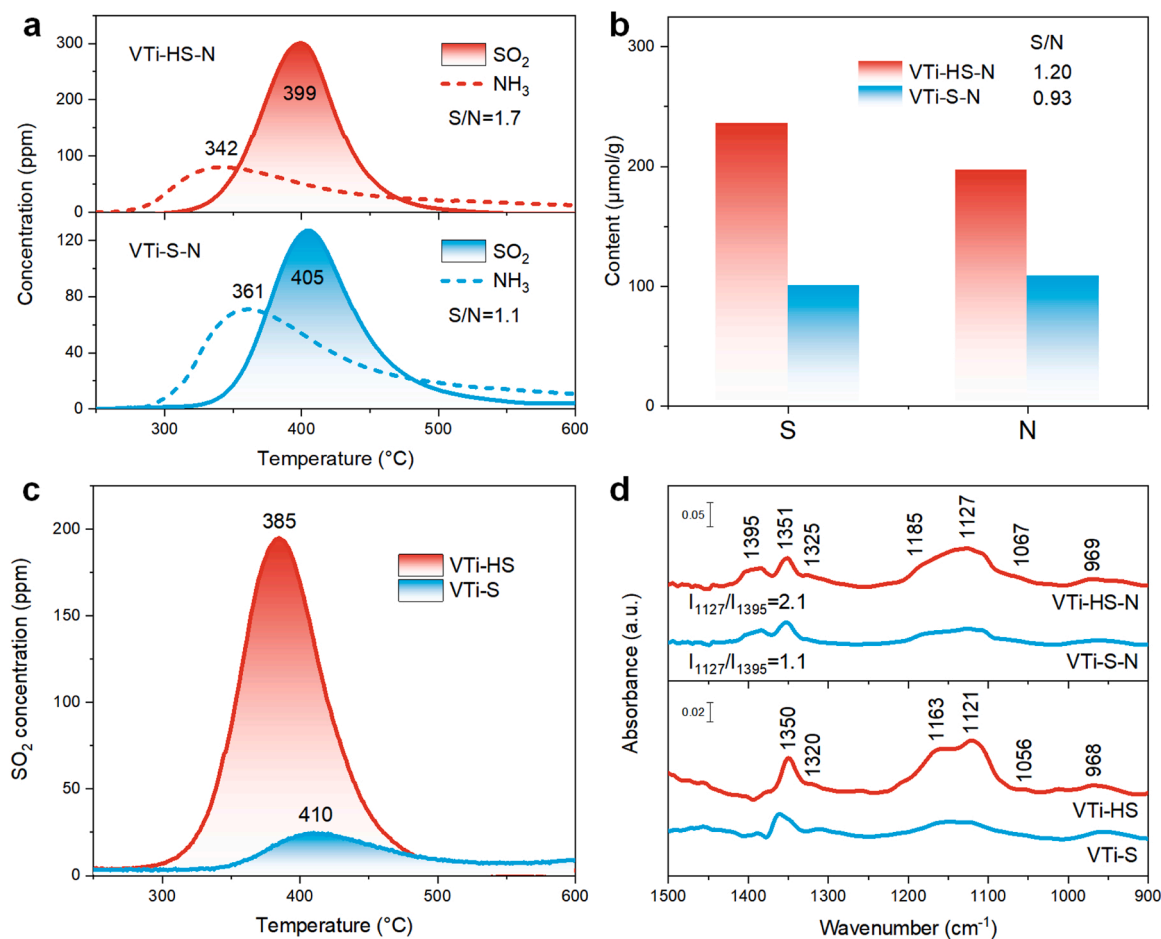


Fig. 2. (a) Temperature-programmed decomposition of sulfur species over VTi-HS-N and VTi-S-N. (b) The sulfur and nitrogen contents of VTi-HS-N and VTi-S-N, which have been subtracted by the contents of S and N in VTi. The sulfur and nitrogen contents were measured by ICP-OES and LECO ONH863 elemental analyzer, respectively. (c) Temperature-programmed decomposition of sulfur species over VTi-HS and VTi-S. (d) FTIR spectra of VTi-HS-N, VTi-S-N, VTi-HS and VTi-S collected at room temperature in air.

oxidation of H₂S, while the sulfates on VTi-S-N may originate from the decomposition of ammonium bisulfate. In other words, the generation of ammonium bisulfate under “NO_x + NH₃ + SO₂ + O₂” was the main reason for the deactivation under SO₂. In contrast, “H₂S + O₂” was the key inducer of H₂S poisoning, and the deposited sulfates were responsible for the sharp deactivation under H₂S. In order to better understand the poisoning mechanism of V₂O₅/TiO₂ by hydrogen sulfide, VTi, VTi-HS, and VTi-S were systematically characterized in the following section.

3.2. Damage to catalyst structure

First, the crystal structure of TiO₂, mainly anatase (~90%), almost remained unchanged after H₂S or SO₂ pretreatment, as shown by the XRD and Raman results of VTi, VTi-HS, and VTi-S (Fig. S5). Besides, most of the converted H₂S (ca. 3000 μmol, Fig. S6) was transformed to SO₂, with only a small amount (ca. 14 μmol) of sulfur species deposited on the catalyst, ranging from 0.7 wt% of VTi to 2.1 wt% of VTi-HS as indicated by ICP results (Table S3). In contrast, the deposited sulfur species under SO₂ pretreatment varied from 0.7 wt% of VTi to 1.3 wt% of VTi-S, less than that under H₂S pretreatment. In this case, both VTi-HS and VTi-S exhibited almost the same BET surface area, pore volume, and vanadium content as fresh VTi (Fig. S7, Table S3). Collectively, XRD, Raman, and BET indicated the poisoning induced neither the destruction of support TiO₂ nor the block of pore structure, so we tried to estimate whether the structure of active species was damaged during H₂S poisoning.

The structure of vanadyl species was detected by a Raman spectrometer at 250 °C in 10% O₂/N₂ (Fig. 3a), where the bands at 1025, 1015, 955, and 930 cm⁻¹ were attributed to the V=O vibration of monomeric, V=O vibration of oligomeric, V–O–V vibration in high polymeric, and V–O–V vibration in oligomeric vanadyl species, respectively [3,29]. The spectra of VTi-HS demonstrated that the monomeric and oligomeric vanadyl species were almost fully destroyed by H₂S. In contrast, parts of monomeric and oligomeric vanadyl species still existed in VTi-S.

Additionally, EPR was conducted to detect the properties of unpaired electrons in VTi, VTi-HS, and VTi-S (Fig. 3b). As the closed-shell electronic structure, no unpaired electrons exist in V⁵⁺ ion (3d⁰), thus making it silent during EPR test, while V⁴⁺ ion (3d¹) had an unpaired electron, rendering it EPR sensitive. The EPR spectra of VTi-HS and VTi-S displayed typical characteristic peaks of V⁴⁺ (I = 7/2, multiplicity 8) [4,30], suggesting that partial V⁵⁺O_x was transformed to V⁴⁺O_x. Moreover, UV–vis was employed to analyze the valence electrons of the catalysts, where a specific electron transition occurred after absorbing ultraviolet-visible light (Fig. 3c). The absorbance at 500–800 nm can be assigned to the d-d transition of reduced vanadyl species (V⁴⁺O_x and/or V³⁺O_x) [31,32]. Combined with the EPR results, it was concluded that vanadyl species was transformed from V⁵⁺O_x to V⁴⁺O_x coupled with the damage of V=O and V–O–V groups, where the transformations were much more substantial under H₂S. However, based on the above results, we could not exclude the generation of unstable species, such as V³⁺O_x and Ti³⁺O_x, because these species could be easily oxidized by O₂ in the

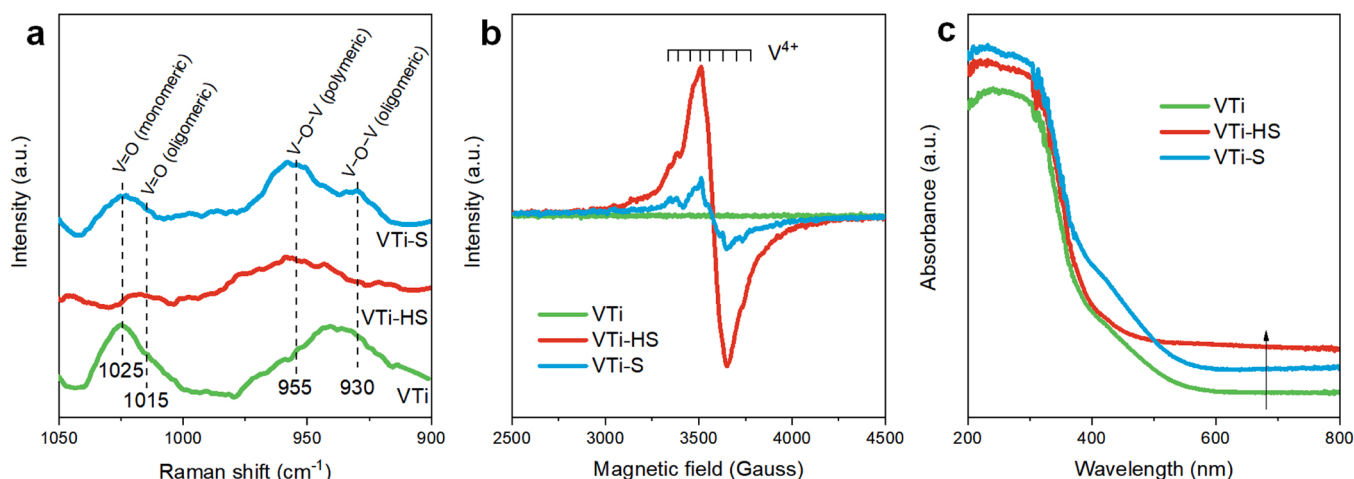


Fig. 3. Raman spectra collected at 250 °C in 10% O₂/N₂ (a), EPR profiles at -148.15 °C (b), and UV-vis spectra at 25 °C (c).

air during the sample transfer process before these ex situ tests.

Moreover, the evolution of valence state during H₂S and SO₂ poisoning was detected by quasi in situ XPS (Fig. 4), where VTi catalyst was pretreated in the reactor of XPS apparatus at 250 °C and then directly transferred to the testing chamber. To exclude the influence of the test procedure, the spectra of VTi pretreated in 10% O₂/N₂ were also collected. As for the spectra of V 2p (Fig. 4a), the peaks at ~517.0, ~515.5, and ~514.0 eV could be ascribed to V⁵⁺, V⁴⁺, and V³⁺, respectively [33,34]. Notably, more low-valence vanadium (V⁴⁺ and V³⁺) existed in VTi-HS and VTi-S than in VTi, demonstrating a significant decrease in the valence state of vanadium.

Furthermore, the spectra of Ti 2p were also collected (Fig. 4b), where the peaks at ~458.9 (~464.8) and ~456.8 (~462.7) eV corresponded to the Ti⁴⁺ and Ti³⁺, respectively [35,36]. Note that the low-valence

vanadium (V⁴⁺ and V³⁺) and low-valence titanium (Ti³⁺) in VTi were probably generated through the loss of oxygen atom during the pre-treatment at 250 °C [3,37]. The low-valence titanium was obviously less in VTi-HS (0%) and VTi-S (17%) than in VTi (29%), indicating an increase in the valence state of titanium. This variation trend of valence state was consistent with ex situ XPS results (Fig. S9).

As for O 1s spectra (Fig. 4c), the peaks at ~530.2 eV were attributed to the lattice oxygen O₂⁻, denoted as O_α, while the peaks at ~531.6 eV might be ascribed to chemisorbed oxygen, surface hydroxyl, adsorbed water, and/or oxygen in sulfate, denoted as O_β [28,38,39]. VTi-HS displayed the most O_β and the most sulfur species (S⁶⁺ and S⁴⁺) as Fig. S8 showed. Thus, the extra O_β was probably mainly derived from the oxygen in the sulfur species, such as the oxygen in S=O and S-OH. After normalization, the S 2p spectra of the deposited sulfur species were

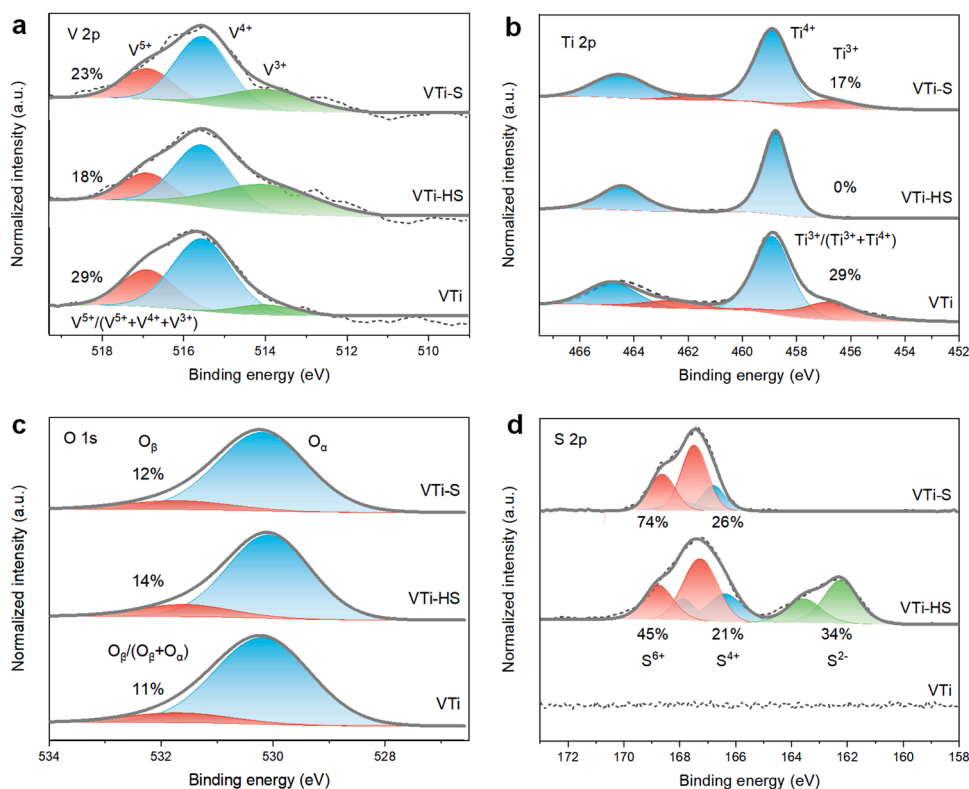


Fig. 4. V 2p (a), Ti 2p (b), O 1s (c), and S 2p (d) quasi in situ XPS spectra of VTi, VTi-HS, and VTi-S. Here, VTi-HS and VTi-S represent the samples pretreated in the reactor of XPS apparatus at 250 °C (details in Section 2.3).

plotted in Fig. 4d. The peaks of VTi-HS at 168.8 (167.4), 167.9 (166.4), and 163.6 (162.2) eV were attributed to the $2p_{1/2}$ ($2p_{3/2}$) of S^{6+} , S^{4+} , and S^{2-} , respectively [40,41], suggesting the existence of sulfate/bisulfate, sulfite/bisulfite, adsorbed SO_2 , and adsorbed H_2S . In contrast, VTi-S displayed peaks corresponding to S^{6+} and S^{4+} , implying the existence of sulfate/bisulfate, sulfite/bisulfite, and adsorbed SO_2 .

According to the spectra of V 2p, Ti 2p, and S 2p, the deposited sulfur species decreased (increased) the valence state of vanadium (titanium), and the changes were more obvious in the valence state of VTi-HS, due to a larger amount and more types of sulfur species on VTi-HS than on VTi-S. Furthermore, we proposed that the generation of extra low-valence vanadium was attributed to the transfer of oxygen atom from vanadium species to sulfur species, where the oxygen in vanadium species could not be replenished fully. This was similar to the generation of V^{4+} in bulk V_2O_5 during H_2S preferential oxidation to sulfur as reported by Axel Löfberg et al. [42]. Then, the high-valence sulfur species transferred to the titanium sites, where the extra oxygen in the sulfur species increased the valence of titanium. This agreed with the report of Xin Tu et al., where the electrons around titanium could be attracted by S=O in sulfate [24]. Collectively, the deposited sulfur species interacted with both vanadium and titanium.

3.3. Generation routes of the sulfates

To further reveal the poisoning mechanism, we detected the intermediates (Fig. 5a, c) and stable deposited sulfur species (Fig. 5b, d) using in situ DRIFTS. After introducing " H_2S+O_2 " or " SO_2+O_2 " (Fig. 5a, c), [44,45] the peaks at 1374, 1357 and 1345 cm^{-1} could be ascribed to gas-phase SO_2 [43] and the band at 1357 cm^{-1} was also probably attributed to weakly adsorbed SO_2 [44], both of which disappeared after O_2/N_2 treatment (Fig. 5b, d). The gas-phase SO_2 in Fig. 5a probably originated from the oxidation and desorption of H_2S , since a large amount of SO_2 was detected when introducing " H_2S+O_2 " (Fig. S3c). The

adsorbed SO_2 contributed to the S^{4+} detected by quasi in situ XPS spectra. Based on above assumption, sulfite should also exist on the catalyst. Here, due to the low amount of sulfite and/or the noise, we did not observe the infrared peaks related to sulfite, whose absorption peaks should appear at 950–800 cm^{-1} [45,46]. Next, the deposited sulfates were analyzed in detail.

As for H_2S poisoning (Fig. 5a, b), the bands at 1283 cm^{-1} could be ascribed to S=O stretching in tridentate sulfate [47,48], and/or deformation of S–O–H in bisulfate [49,50]. Besides, the peak at 1283 cm^{-1} might also originated from elemental sulfur allotropes [51], which could generate from the reaction between H_2S and SO_2 [52]. In Fig. 5b, the peak at 1283 cm^{-1} decreased gradually, coupled with the gradual appearance of the peaks at 1372 and 1310 cm^{-1} . Considering the observed dehydration process (Fig. S10), the peaks at 1283 cm^{-1} were probably derived from bisulfate mainly. Meanwhile, the peaks at 1372 and 1310 cm^{-1} could be ascribed to tridentate [28,49] and/or bidentate sulfates [28,53]. Besides, the polymeric sulfates, such as $S_2O_7^{2-}$, also displayed the peaks around 1370 cm^{-1} [54,55]. Moreover, the broad peak around 1150 cm^{-1} could be assigned to the symmetrical stretching vibration of O=S=O in bidentate sulfate [24,28], while the broad shoulder peak in 1080–1040 cm^{-1} could be ascribed to the asymmetrical stretching of S–O in O–S–O binding to metal (Ti and/or V, possibly) [25,56,57]. Additionally, the negative peak at 1033 cm^{-1} (Fig. 5a, b) might be attributed to the stretching vibration of the original V=O consumed during the test [3]. Taken together, various sulfur species were generated during H_2S poisoning, including adsorbed SO_2 , bisulfate, bidentate sulfate, tridentate sulfate, and/or polymeric sulfate, where bisulfate was unstable and tended to transform to other sulfates.

As for SO_2 poisoning (Fig. 5c, d), no obvious peaks appeared at 1283 cm^{-1} , indicating almost no bisulfates were generated. Besides, the peaks at 1373, 1316, 1155, and 1078 cm^{-1} were far lower under SO_2 than under H_2S , indicating that the final deposited species were of the same type under both H_2S and SO_2 , but with a much less amount under

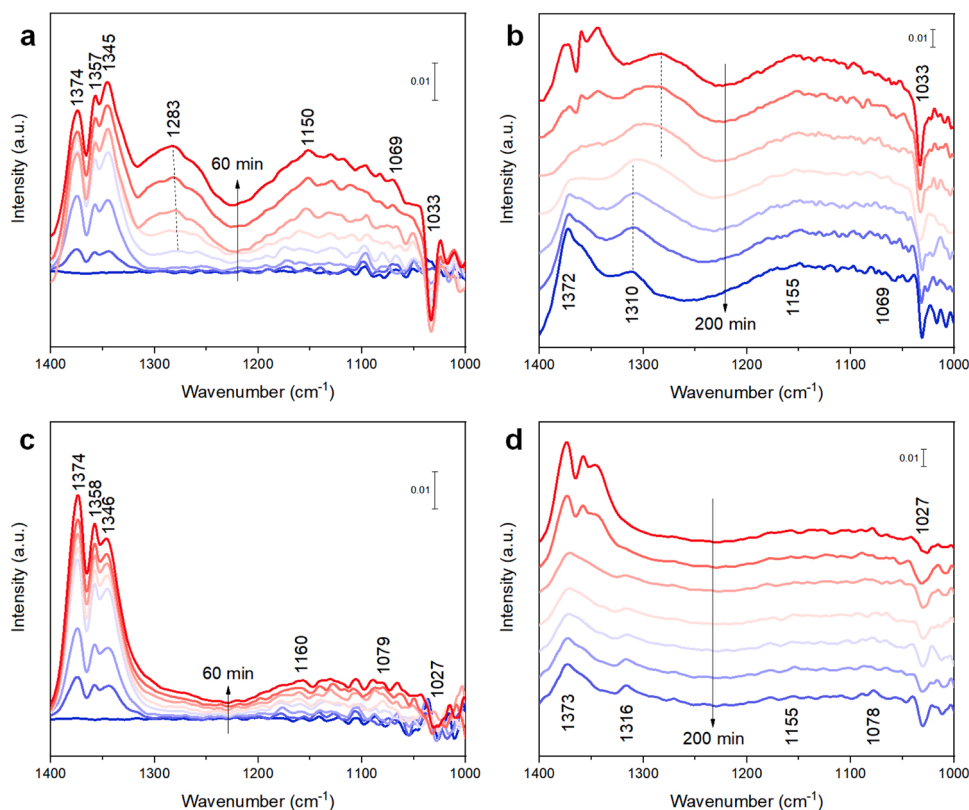


Fig. 5. Time-resolved in situ DRIFTS spectra collected at 250 °C of (a) H_2S poisoning (5000 ppm H_2S , 10% O_2), followed by (b) 10% O_2/N_2 purging over VTi. The spectra of (c) SO_2 poisoning (5000 ppm SO_2 , 10% O_2), followed by (d) 10% O_2/N_2 purging over VTi.

SO₂. Furthermore, the final spectra at 200 min in Fig. 5b, d were close to the FTIR (Fig. 2d) spectra, confirming the deposition of various sulfates, including bidentate sulfate, tridentate sulfate, and/or polymeric sulfate.

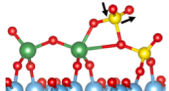
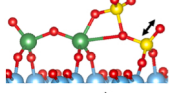
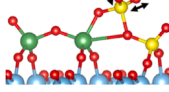
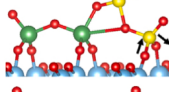
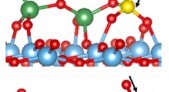
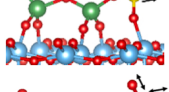
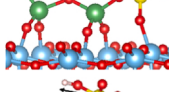
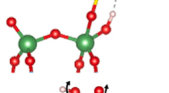
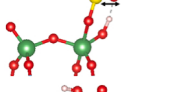
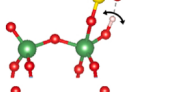
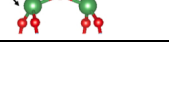
The sulfates deposited during H₂S poisoning are probably generated from H₂S directly and/or from the SO₂ born of H₂S. As discussed above, the deposited sulfur species on VTi-HS were far different from that on VTi-S in terms of type and amount. Thus, the deposited sulfates were deduced to be mainly generated from H₂S directly. To verify the reasonability of this speculation, DFT simulations were conducted to obtain the intermediates and calculate their free energy. The model of VTi was described in Section 2.4, where a V₂O₇ cluster represented the SCR active site, i.e., oligomeric vanadyl species [6,23]. Based on the results of XPS and DRIFTS, several configurations of the sulfates were proposed and optimized (Table 1, Table S4). The calculated vibration frequencies of tridentate and bidentate sulfates were close to previous reports [48,58], verifying the reasonability of our calculations. Here, the calculated frequencies of the configurations in Table 1, especially polymeric sulfate (tridentate-bidentate), were close to the results obtained by DRIFTS, verifying the reasonability of these configurations. Note that the frequencies of similar vibrations (such as asymmetrical stretching of O=S=O) in polymeric sulfate were different from those in

bidentate sulfate, probably due to the vibrational coupling between the adjacent O=S=O groups [55]. Importantly, the exact match between the calculated and measured frequencies revealed polymeric sulfate as the main final deposited species.

Furthermore, several routes of H₂S oxidation and deposition were proposed with sulfates or SO₂ as the products (Fig. S11–16). Compared with other sulfates (Fig. S11–12), polymeric sulfate (Fig. 6a) was supposed to be the most energetically favorable due to the lowest free energy of intermediates and final products [6,29], verifying polymeric sulfate was a representative deposited sulfur species. Fig. 6a displays the route of H₂S transformation to polymeric sulfate, where an H₂S molecule was adsorbed on the V=O group and a hydrogen atom transferred to vanadyl species (B→C), forming one HO–V–SH structure. Then, the V–SH reacted with gaseous O₂ molecule to generate V–OOSH group, which was then attacked by O₂ (D→E) and transformed to bisulfate V–SO₄H (F→G). After dehydration and transformation (H→I), bidentate sulfate was generated. Next, through oxidation of another H₂S molecule, the adjacent bisulfate/sulfate/sulfite interacted with each other to form polymeric sulfate ultimately (I→J). The generation route of sulfite would be proposed in the following context.

As for the generation of polymeric sulfate from SO₂, a feasible

Table 1
The frequencies obtained by DRIFTS and DFT calculation.

Species	Bands	Frequency (cm ⁻¹) In situ DRIFTS	Vibrations	Frequency (cm ⁻¹) DFT calculation
Polymeric sulfate (Tridentate- Bidentate)	O=S=O Asymmetrical	1372[54,55]		1358
	S=O	1310[47,48]		1302
	O=S=O Symmetrical	1155[59]		1158
	O–S–O Asymmetrical	1069[24,56,57]		1071
Tridentate sulfate	S=O	1283[47,48]		1281[48]
Bidentate sulfate	O=S=O Asymmetrical	1310[53]		1305[58]
	O=S=O Symmetrical	1155[59]		1127[58]
Bisulfate	OH	3655[33,60]		3662
	S–O–H Bending	1283[49,50]		1290
	V–O–H Bending	1151		1130
V ₂ O ₇	V=O	1033[3]		1029

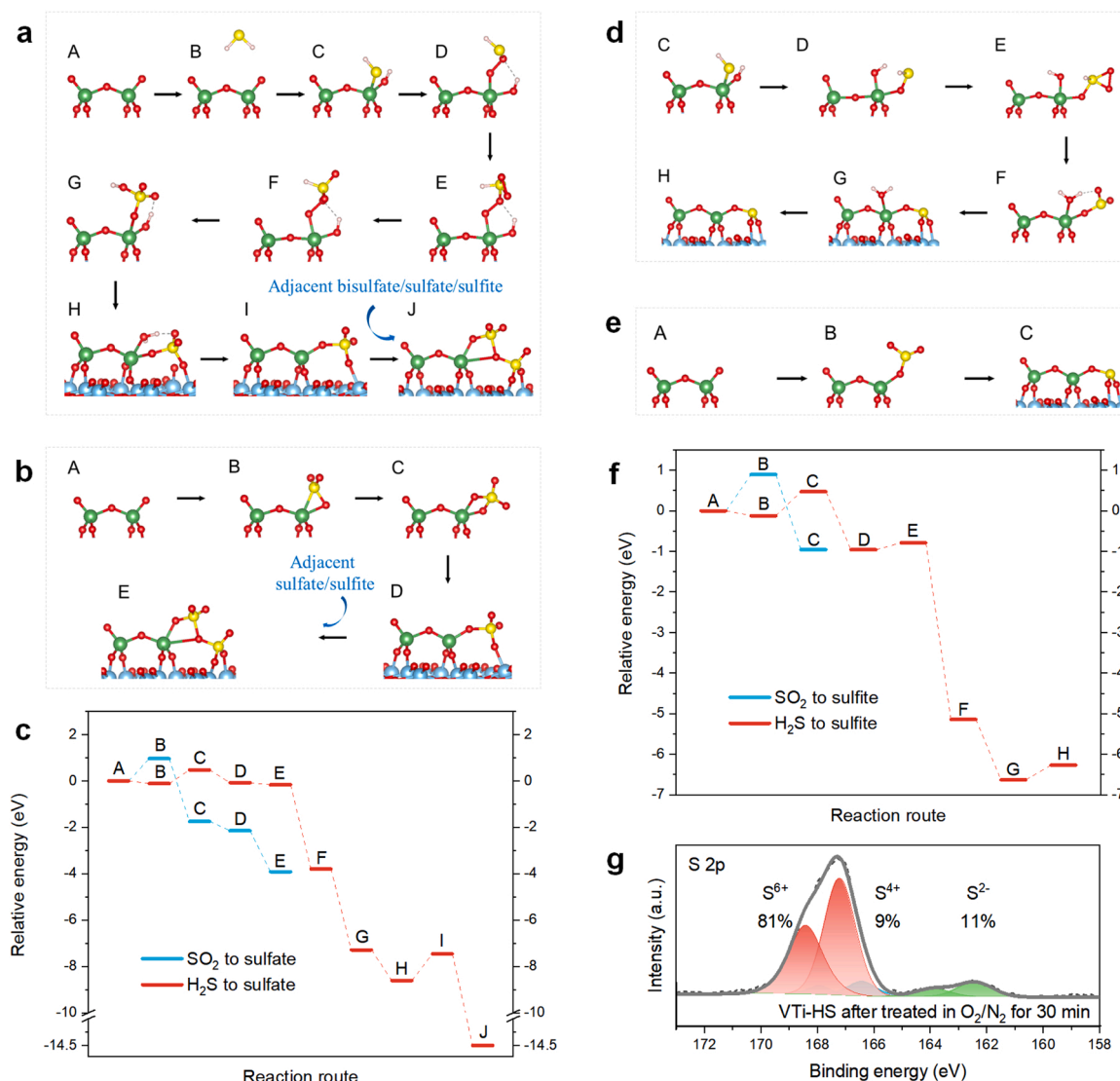


Fig. 6. (a) A proposed H₂S poisoning route, where polymeric sulfate was generated. (b) A proposed route from SO₂ to polymeric sulfate. Green, red, yellow, pink, and blue balls represented vanadium, oxygen, sulfur, hydrogen, and titanium atoms, respectively. (c) Energy profiles of the poisoning routes in Fig. 6a-b. (d) A proposed route from H₂S to sulfite. (e) A proposed route from SO₂ to sulfite. (f) Energy profiles of the sulfite generation routes in Fig. 6d-e. (g) S 2p quasi in situ XPS spectra of VTi-HS with further treatment in O₂/N₂ for 30 min. Here, VTi-HS represents the samples pretreated in the reactor of XPS apparatus at 250 °C (details in Section 2.3).

poisoning route was also proposed (Fig. 6b). Briefly, the SO₂ molecule attacked the V=O group and formed a bidentate sulfite-like group with a V-S bond and a V-O bond, which was further oxidized by surface reactive oxygen and converted to VOSO₄-like bidentate sulfate (A→C). Next, one V-O bond was broken and one V-O-Ti was formed, generating bidentate sulfate (C→D). Subsequently, through oxidation of another SO₂ molecule, the adjacent sulfate/sulfite interacted with each other to form polymeric sulfate ultimately (D→E). As Fig. 6c showed, the free energy of both intermediates and final products from SO₂ was obviously higher than that from H₂S, supporting that the deposited sulfur species was distinctly less under SO₂ than under H₂S. These results also verified that the sulfates deposited under H₂S poisoning were mainly generated from H₂S directly, which were more energetically favorable than the sulfates derived from the SO₂ born of H₂S.

The proposed routes from H₂S or SO₂ to sulfite were plotted in Fig. 6d-e. As for the route of H₂S to sulfite (Fig. 6d), the configuration C (V-SH) was identical to that in Fig. 6a. Next, the V-SH was oxidized by surface reactive oxygen and converted to V-OSH group (C→E), which was further oxidized to form sulfite and adsorbed H₂O (E→F). After dehydration and transformation, a tridentate sulfite was formed (F→H).

Note that we had tried to construct several configurations containing HSO₃²⁻, but these structures could not exist after geometry optimization, implying the absence of HSO₃²⁻ on the catalyst. As for the route of SO₂ to sulfite (Fig. 6e), the SO₂ molecule attacked the V=O group and formed a monodentate sulfite, which further transferred to titanium and formed sulfite (A→C). Thereafter, the sulfite could participate in the formation of polymeric sulfate. As shown in Fig. 6f, the free energy of both intermediates and final products was also higher during the generation of sulfite from SO₂ than from H₂S. This result implied the sulfite can be more easily formed from H₂S than from SO₂, which also led to the quick deposition of polymeric sulfate under H₂S. Besides, as shown by the quasi in situ XPS spectra (Fig. 4d and Fig. 6g), after oxidation in O₂/N₂ for 30 min, the ratio of S⁴⁺ decreased, while the ratio of S⁶⁺ increased, indicating the conversion of S⁴⁺ to S⁶⁺. This can verify the speculation that sulfite participates in the formation of polymeric sulfate.

Apparently, with the formation of polymeric sulfate, V=O was converted to V-O-S (Fig. 6a), which should be the key reason for SCR activity decline under H₂S poisoning. Here, we took the V-O-S bond as an example to study the impact of H₂S on the electronic structure of vanadium and oxygen atoms in the V=O group. As shown by the charge

difference distribution in Fig. 7a, after V–O–S formation, the charge density around vanadium (titanium) atoms increased (decreased), which was in line with the XPS results. In Fig. 7b, a decrease was observed in the charge density between V_1 and O_1 atoms, indicating a reduction in the double-bond character of V_1-O_1 . Moreover, we calculated the partial density of states (PDOS) of V_1 and O_1 in the V–O–S bond and their corresponding atoms in VTi model (Fig. 7c). Evidently, due to the electronic coupling with S-p, the electrons in O-p and V-d orbitals tended to locate at a lower energy in VTi-HS. Furthermore, the unoccupied orbitals of VTi-HS also shifted to a lower energy, but the shift value was less than that of occupied orbitals, i.e., the energy gap was widened from 2.36 eV to 2.77 eV. Therefore, the charge transfer between occupied and unoccupied orbitals was inhibited, leading to a lower reactivity of V–O–S than $V=O$ [5,61].

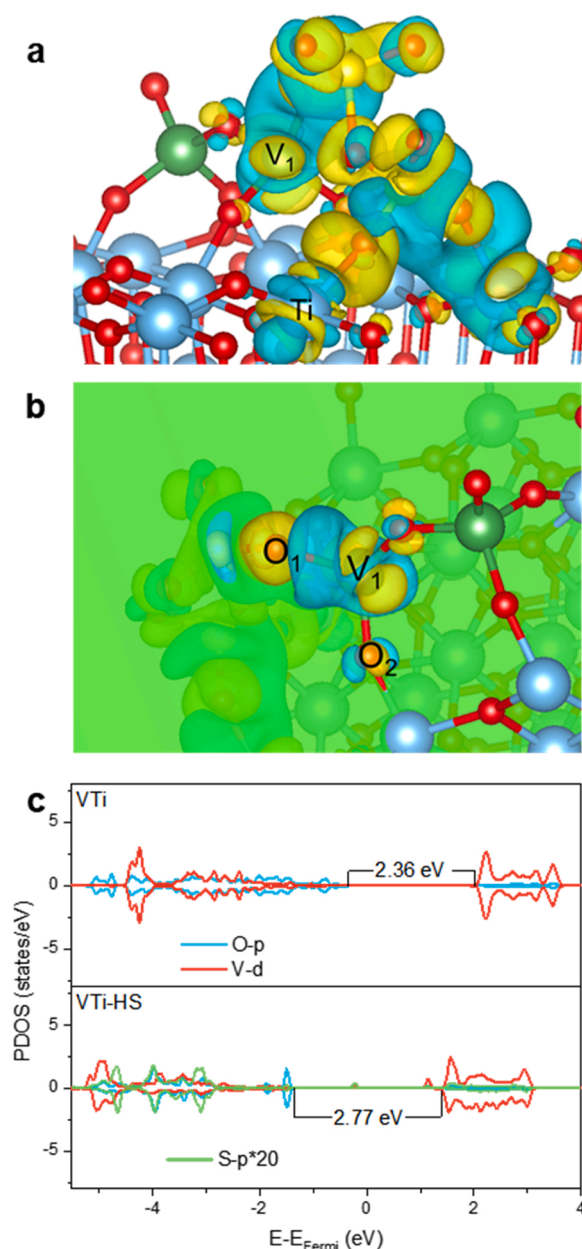


Fig. 7. (a–b) The charge difference distribution between polymeric sulfate and VTi from different visual angles with the isosurface at $0.020 \text{ e} \cdot \text{\AA}^{-3}$. The yellow (blue) isosurface represents the increase (decrease) of charge density. (c) PDOS of V and O atoms in the V=O (V–O–S) bond on the model of VTi (VTi-HS).

3.4. Inhibition on NH_3 activation

SCR over VTi catalyst mainly proceeds through Eley-Rideal (E-R) mechanism, where gaseous NO reacts with adsorbed NH_3 to form N_2 and H_2O [22,62], demonstrating a vital role of NH_3 adsorption and activation in SCR. Here, DRIFTS was conducted to analyze the influence of sulfates on the capability of VTi catalyst for NH_3 adsorption (Fig. S17). The bands at 1422 and $1237(1246) \text{ cm}^{-1}$ were ascribed to the NH_3 adsorbed on Brønsted acid sites (NH_4^+) and Lewis acid sites (NH_3^+), respectively [5,22]. As shown in Fig. S17, both NH_4^+ and NH_3^+ increased after H_2S or SO_2 poisoning. However, the deposited sulfates and the destroyed vanadium sites were also potential sites for NH_3 adsorption, so the reactivity of the NH_4^+ and NH_3^+ needed further verification. Fig. 8a–b show the reaction between adsorbed NH_3 and gaseous NO. After introducing $\text{NO} + \text{O}_2$, the NH_3 adsorbed on VTi vanished followed by adsorbed NO_2 and/or nitrate ($1628, 1602$, and 1372 cm^{-1}) appeared [22,63], demonstrating that the SCR over VTi mainly followed E-R mechanism [22,64]. In sharp contrast, the NH_3 adsorbed on VTi-HS remained almost unchanged. Furthermore, we calculated the normalized intensity of peaks corresponding to NH_4^+ and NH_3^+ , and their variation trend with time was plotted in Fig. 8c. Obviously, the consumption of both NH_4^+ and NH_3^+ was much slower over VTi-HS than over VTi, demonstrating that the reaction between adsorbed NH_3 and gaseous NO was significantly retarded after H_2S poisoning. Likewise, the reactivity of the NH_3 adsorbed on VTi-S was also inhibited to some content (Fig. S17b–c).

Usually, NH_3 activation, namely the transfer of a hydrogen atom of NH_3 to $V=O$ to form a V–OH structure, is believed to be the rate-determining step in SCR reaction [16,22]. In the present study, the reaction barrier of NH_3 activation was evaluated by analyzing the transition states. First, the final construction of VTi (C in Fig. 8d) ($\text{H}_2\text{N} - \text{V} - \text{OH}$) was established on $V=O$ due to its relative high reactivity [5,22], followed by optimizing the corresponding initial construction (A in Fig. 8d) and searching the transition states by Dimer method, where the Gibbs free energy was corrected to the value at 250°C . Here, the reaction barrier of NH_3 activation was calculated as 1.38 eV, which was close to the previous report [22]. As for VTi-HS, the final construction on V–O–S ($\text{H}_2\text{N} - \text{V} - \text{OH} - \text{S}$) was built, but this construction could not exist after geometry optimization, agreeing well with the electronic structure analysis that the reactivity of $V=O$ was inhibited. Meanwhile, the final construction on V–O–Ti was also considered (F in Fig. 8d), but this construction was also unable to exist after geometry optimization, indicating NH_3 activation was fully inhibited by polymeric sulfate. These results were consistent with the sharp decline of SCR activity caused by H_2S (Fig. 1a).

3.5. Mechanism of the deactivation

Based on the analysis of deactivation behaviors under various gas compositions and related characterizations (decomposition test, elemental analysis, and FTIR), the generation of ammonium bisulfate (ABS) under “ $\text{NO}_x + \text{NH}_3 + \text{SO}_2 + \text{O}_2$ ” was the main contributor to the deactivation under SO_2 , while “ $\text{H}_2\text{S} + \text{O}_2$ ” was the key inducer of H_2S poisoning and the deposited sulfates were responsible for the sharp deactivation (Scheme 1).

To better understand the mechanism of H_2S poisoning, a comparative study was performed by characterizing the samples pretreated under “ $\text{H}_2\text{S} + \text{O}_2$ ” (VTi-HS) and “ $\text{SO}_2 + \text{O}_2$ ” (VTi-S) in detail. Most of the converted H_2S was transformed to SO_2 , with only a small amount of sulfur species deposited on VTi-HS. These deposited sulfur species seriously damaged the active sites of SCR, especially monomeric and oligomeric vanadyl species, with the damage being much more substantial in VTi-HS than in VTi-S. Quasi in situ XPS showed the presence of both S^{6+} and S^{4+} during poisoning, suggesting the existence of sulfite. Besides, the spectra of V 2p and S 2p revealed the interaction of sulfur species with both vanadium and titanium.

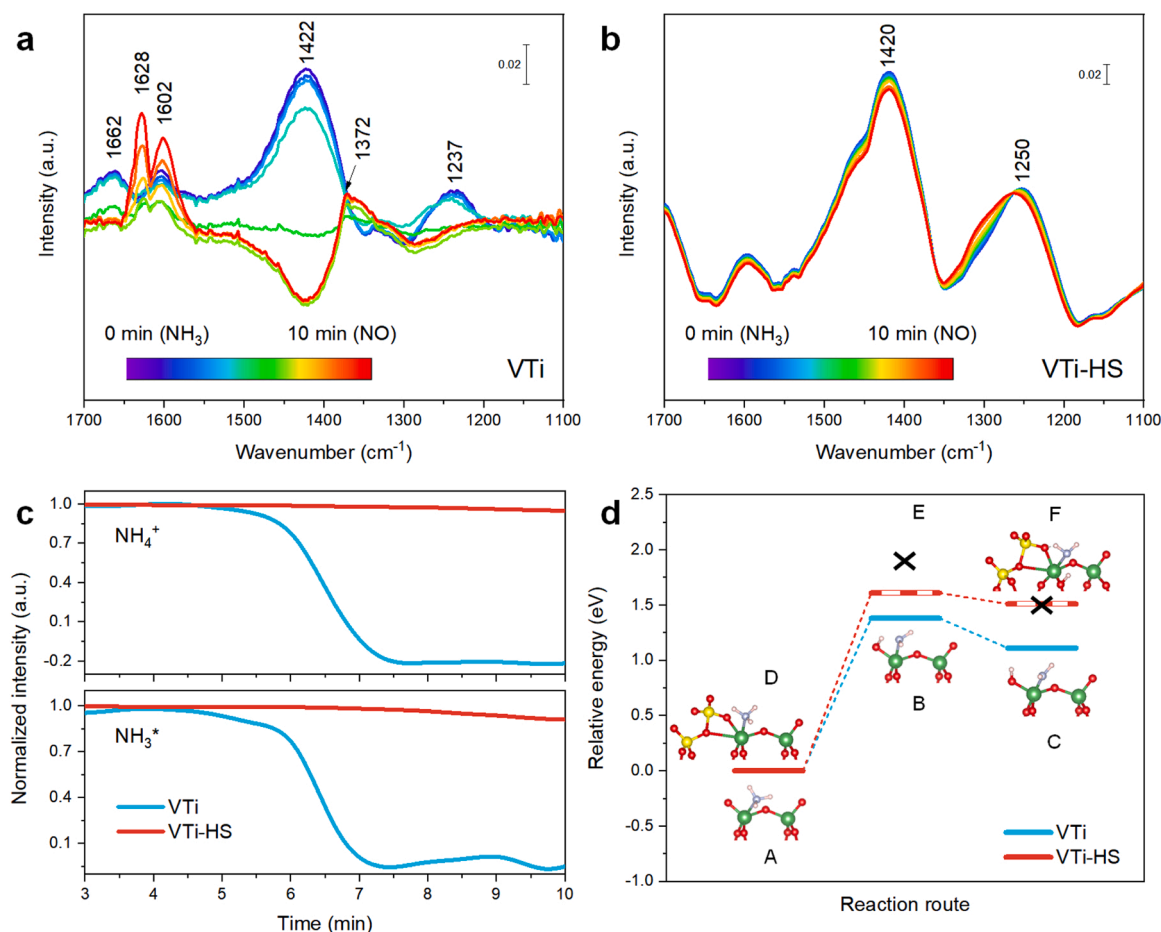
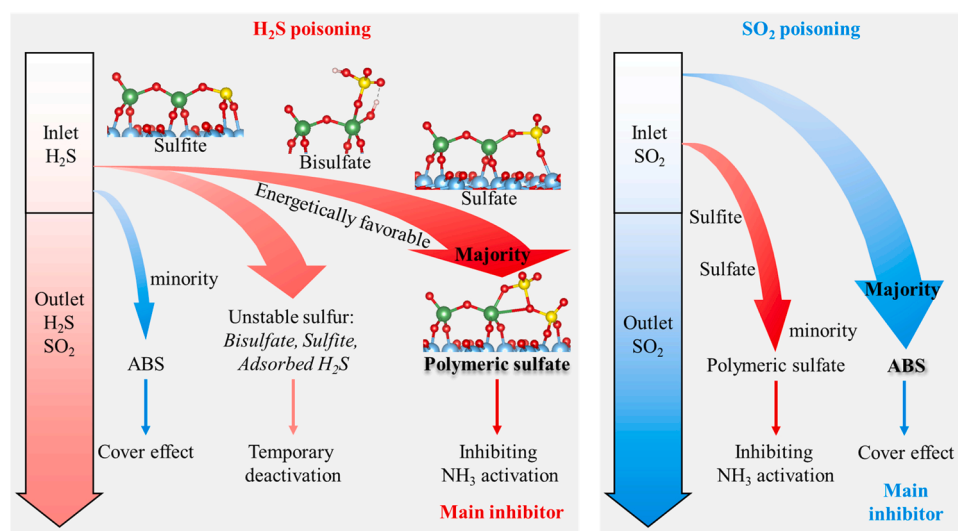


Fig. 8. Time-resolved in situ DRIFTS spectra collected at 250 °C of NO reacted with previously adsorbed NH₃ over VTi (a) and VTi-HS (b). The time-varying normalized intensity of NH₄⁺ and NH₃^{*} over VTi and VTi-HS (c). Gibbs free energy profile of NH₃ dehydration over VTi and VTi-HS at 250 °C (d).



Scheme 1. The deactivation mechanism of VTi under H₂S or SO₂ poisoning.

In situ DRIFTS showed the generation of various sulfur species during H₂S poisoning, including SO₂, bisulfate, bidentate sulfate, tridentate sulfate, and/or polymeric sulfate, where bisulfate (HSO₄²⁻) was unstable and tended to transform to other sulfates. Under SO₂, bidentate sulfate, tridentate sulfate, and/or polymeric sulfate were also generated, but their amount was less than that under H₂S. Frequency calculations and

DRIFTS revealed polymeric sulfate as the main final deposited species. Then, several feasible poisoning routes from H₂S or SO₂ to sulfite and sulfates were investigated by DFT simulations, with the free energy of both intermediates and final products were obviously higher under SO₂ than under H₂S. These results supported the deposition of a large amount of sulfates was deposited under H₂S poisoning.

Charge difference distribution between polymeric sulfate and catalyst showed that the vanadium (titanium) atoms gained (lost) electrons, agreeing with the EPR, UV-vis, and XPS results, further confirming the reasonability of this configuration. Then, we took polymeric sulfate as an example to investigate how the SCR reaction was inhibited. With this sulfate, the V=O in oligomeric vanadyl species was transformed to V-O-S, which lowered the charge density in V-O bond and widened the energy gap, thus inhibiting the charge transfer between occupied and unoccupied orbitals and finally suppressing NH₃ activation and SCR activity. Besides, the sulfates on the catalyst could be removed by thermal regeneration to achieve activity recovery (Fig. S18), confirming sulfates as the main inducer of the sharp activity decline under H₂S.

With respect to the activity recovery stage after stopping H₂S injection in Fig. 1a, we proposed two possible explanations. First, the massive sulfite and adsorbed H₂S were transformed to gaseous SO₂, leading to the release of some vanadium sites, which can be supported by quasi in situ XPS (Fig. 4d and Fig. 6g). Second, bisulfate was transformed to polymeric sulfate, enabling partial recovery of the active sites recovered, as evidenced by DRIFTS (Fig. 5b). Collectively, bisulfate, sulfite, and adsorbed H₂S were the unstable factors inhibiting SCR activity during H₂S poisoning.

4. Conclusions

In summary, we comparatively investigated the V₂O₅/TiO₂ deactivation under H₂S or SO₂, where the deactivation rate under H₂S was almost six-fold that under SO₂ in the initial stage (activity from ~70% to ~40%). Ammonium bisulfate was the main reason for the deactivation under SO₂ while deposited sulfates were responsible for the sharp deactivation under H₂S. Systematic characterizations and frequency calculation revealed polymeric sulfate as the main sulfate deposited under H₂S. Additionally, several poisoning routes were proposed, with the generation of polymeric sulfate being more energetically favorable under H₂S, resulting in the much more deposited sulfates under H₂S than under SO₂. The polymeric sulfate destroyed the monomeric and oligomeric vanadyl species, with the V=O being transformed to V-O-S. Specifically, this sulfate inhibited the charge transfer between the occupied and unoccupied orbitals of V=O, thus suppressing the NH₃ activation and SCR activity. Moreover, we proposed that bisulfate, sulfite, and adsorbed H₂S led to the temporary deactivation during H₂S poisoning. The above poisoning mechanisms could provide new insights into the deactivation of SCR catalysts and the development of sulfur-resistant catalysts.

CRedit authorship contribution statement

Rongqiang Yin: Conceptualization, Methodology, Investigation, Data curation, Writing – original draft. **Jianjun Chen:** Supervision, Funding acquisition, Conceptualization, Writing – review & editing. **Liang Shan:** Investigation, Data curation. **Jianqiang Shi:** Methodology. **Kun Yang:** Methodology. **Hao Liu:** Discussion. **Junhua Li:** Supervision, Project administration, Funding acquisition, Writing – review & editing.

Declaration of Competing Interest

The authors declare that they have no known competing financial interests or personal relationships that could have appeared to influence the work reported in this paper.

Data Availability

Data will be made available on request.

Acknowledgements

This work was financially supported by the National Natural Science

Foundation of China (21936005 & 52070114) and the National Key R&D program of China (2022YFC3701600).

Appendix A. Supporting information

Supplementary data associated with this article can be found in the online version at doi:10.1016/j.apcatb.2023.122529.

References

- [1] K. Guo, J. Ji, W. Song, J. Sun, C. Tang, L. Dong, Conquering ammonium bisulfate poison over low-temperature NH₃-SCR catalysts: a critical review, *Appl. Catal. B* 297 (2021), 120388.
- [2] L. Han, S. Cai, M. Gao, J. Hasegawa, P. Wang, J. Zhang, L. Shi, D. Zhang, Selective catalytic reduction of NO_x with NH₃ by using novel catalysts: State of the art and future prospects, *Chem. Rev.* 119 (2019) 10916–10976.
- [3] Y. Ganjkanlou, T.V.W. Janssens, P.N.R. Venneström, L. Mino, M.C. Paganini, M. Signorile, S. Bordiga, G. Berlier, Location and activity of VO_x species on TiO₂ particles for NH₃-SCR catalysis, *Appl. Catal. B* 278 (2020), 119337.
- [4] N.R. Jaegers, J. Lai, Y. He, E. Walter, D.A. Dixon, M. Vasiliu, Y. Chen, C. Wang, M. Y. Hu, K.T. Mueller, I.E. Wachs, Y. Wang, J.Z. Hu, Mechanism by which tungsten oxide promotes the activity of supported V₂O₅/TiO₂ catalysts for NO_x abatement: structural effects revealed by ⁵¹V MAS NMR spectroscopy, *Angew. Chem. Int. Ed.* 58 (2019) 2–10.
- [5] S. Xiong, J. Chen, H. Liu, X. Chen, W. Si, Z. Gong, Y. Peng, J. Li, Like cures like: detoxification effect between alkali metals and sulfur over the V₂O₅/TiO₂ deNO_x catalyst, *Environ. Sci. Technol.* 56 (2022) 3739–3747.
- [6] G. Chen, S. Xiong, X. Chen, X. Chu, R. Yin, C. Liu, J. Chen, J. Li, Penetration of arsenic and deactivation of a honeycomb V₂O₅-WO₃/TiO₂ catalyst in a glass furnace, *Environ. Sci. Technol.* 55 (2021) 11368–11374.
- [7] I. Song, S.W. Jeon, H. Lee, D.H. Kim, Tailoring the mechanochemical interaction between vanadium oxides and zeolite for sulfur-resistant deNO_x catalysts, *Appl. Catal. B* 316 (2022), 121672.
- [8] I. Song, H. Lee, S.W. Jeon, I.A.M. Ibrahim, J. Kim, Y. Byun, D.J. Koh, J.W. Han, D. Kim, Simple physical mixing of zeolite prevents sulfur deactivation of vanadia catalysts for NO_x removal, *Nat. Commun.* 12 (2021) 9.
- [9] T. Yamamoto, M. Tayakout-Fayolle, C. Geantet, Gas-phase removal of hydrogen sulfide using iron oxyhydroxide at low temperature: measurement of breakthrough curve and modeling of sulfidation mechanism, *Chem. Eng. J.* 262 (2015) 702–709.
- [10] G. García, E. Cascarosa, J. Ábrego, A. Gonzalo, J.L. Sánchez, Use of different residues for high temperature desulphurisation of gasification gas, *Chem. Eng. J.* 174 (2011) 644–651.
- [11] J.P. Zhang, Y. Sun, M.W. Woo, L. Zhang, K.Z. Xu, Preparation of steam activated carbon from black liquor by flue gas precipitation and its performance in hydrogen sulfide removal: experimental and simulation works, *J. Taiwan Inst. Chem. Eng.* 59 (2016) 395–404.
- [12] J.Z. Cai, D. Li, D.G. Chen, Z.S. Li, NO_x and H₂S formation in the reductive zone of air-staged combustion of pulverized blended coals, *Front. Energy* 15 (2020) 4–13.
- [13] W.K. Ahmed, T.A. Abed, A.Q. Salam, K.S. Reza, M.T. Mahdiy, M.T. Chaichan, Environmental impact of using generators in the university of technology in Baghdad, Iraq, *J. Therm. Eng.* 6 (2020) 272–281.
- [14] N. Otsuka, 1.18 - Fireside Corrosion, in: B. Cottis, M. Graham, R. Lindsay, S. Lyon, T. Richardson, D. Scantlebury, H. Stott (Eds.), *Shreir's Corrosion*, Elsevier, Oxford, 2010, pp. 457–481.
- [15] L. Shan, R. Yin, B. Wang, Q. Zhou, Z. Wang, J. Xu, L. Meng, J. Chen, Z. Zhang, J. Li, The performance of 3D graded catalytic ceramic-fiber filter and the pilot test of glass furnace, *Energy Environ. Prot. (China)* 35 (2021) 13–17.
- [16] J. Lai, I.E. Wachs, A perspective on the selective catalytic reduction (SCR) of NO with NH₃ by supported V₂O₅-WO₃/TiO₂ catalysts, *ACS Catal.* 8 (2018) 6537–6551.
- [17] X. Hu, J. Chen, W. Qu, R. Liu, D. Xu, Z. Ma, X. Tang, Sulfur-resistant ceria-based low-temperature SCR catalysts with the non-bulk electronic states of ceria, *Environ. Sci. Technol.* 55 (2021) 5435–5441.
- [18] H. Liu, Z. Fan, C. Sun, S. Yu, S. Feng, W. Chen, D. Chen, C. Tang, F. Gao, L. Dong, Improved activity and significant SO₂ tolerance of samarium modified CeO₂-TiO₂ catalyst for NO selective catalytic reduction with NH₃, *Appl. Catal. B* 244 (2019) 671–683.
- [19] J.H. Yang, H.J. Lee, H.S. Lee, S.C. Jeon, Y.S. Han, Precise control of heat-treatment conditions to improve the catalytic performance of V₂O₅/TiO₂ for H₂S removal, *J. Hazard. Mater.* 416 (2021), 125974.
- [20] H. Eom, S.M. Lee, H. Kang, Y.H. Lee, S.W. Chang, S.S. Kim, Effect of VO_x surface density and structure on VO_x/TiO₂ catalysts for H₂S selective oxidation reaction, *J. Ind. Eng. Chem.* 92 (2020) 252–262.
- [21] F. Quan, N. Yan, Z. Qu, S. Zhao, Preparation of mid-low temperature SCR catalysts used in coking flue gas and the mechanism of H₂S influence, *Environ. Sci. Technol. (China)* 39 (2016) 53–58,63.
- [22] G. He, Z. Lian, Y. Yu, Y. Yang, K. Liu, X. Shi, Z. Yan, W. Shan, H. He, Polymeric vanadyl species determine the low-temperature activity of V-based catalysts for the SCR of NO_x with NH₃, *Sci. Adv.* 4 (2018) eaau4637.
- [23] J. Chen, R. Yin, G. Chen, J. Lang, X. Chen, X. Chu, J. Li, Selective capture of Ti₂O from flue gas with formation of p-n junction on V₂O₅-WO₃/TiO₂ catalyst under working conditions, *Green. Energy Environ.* (2022).
- [24] X. Wang, X. Du, S. Liu, G. Yang, Y. Chen, L. Zhang, X. Tu, Understanding the deposition and reaction mechanism of ammonium bisulfate on a vanadia SCR

- catalyst: a combined DFT and experimental study, *Appl. Catal. B* 260 (2020), 118168.
- [25] T. Tong, J.J. Chen, S.C. Xiong, W.H. Yang, Q.L. Yang, L.J. Yang, Y. Peng, Z.M. Liu, J.H. Li, Vanadium-density-dependent thermal decomposition of NH_4HSO_4 on $\text{V}_2\text{O}_5/\text{TiO}_2$ SCR catalysts, *Catal. Sci. Technol.* 9 (2019) 3779–3787.
- [26] D. Ye, R. Qu, H. Song, X. Gao, Z. Luo, M. Ni, K. Cen, New insights into the various decomposition and reactivity behaviors of NH_4HSO_4 with NO on $\text{V}_2\text{O}_5/\text{TiO}_2$ catalyst surfaces, *Chem. Eng. J.* 283 (2016) 846–854.
- [27] X. Guo, C. Bartholomew, W. Hecker, L.L. Baxter, Effects of sulfate species on $\text{V}_2\text{O}_5/\text{TiO}_2$ SCR catalysts in coal and biomass-fired systems, *Appl. Catal. B* 92 (2009) 30–40.
- [28] J.P. Chen, R.T. Yang, Selective catalytic reduction of NO with NH_3 on $\text{SO}_4^{2-}/\text{TiO}_2$ superacid catalyst, *J. Catal.* 139 (1993) 277–288.
- [29] Z. Lian, J. Wei, W. Shan, Y. Yu, P.M. Radjenovic, H. Zhang, G. He, F. Liu, J. Li, Z. Tian, H. He, Adsorption-induced active vanadium species facilitate excellent performance in low-temperature catalytic NO_x abatement, *J. Am. Chem. Soc.* 143 (2021) 10454–10461.
- [30] S. Zhang, H. Li, Q. Zhong, Promotional effect of F-doped $\text{V}_2\text{O}_5\text{--WO}_3/\text{TiO}_2$ catalyst for $\text{NH}_3\text{--SCR}$ of NO at low-temperature, *Appl. Catal. A*, 435–436 (2012) 156–162.
- [31] L.J. Burcham, G. Deo, X. Gao, I.E. Wachs, In situ IR, Raman, and UV-Vis DRS spectroscopy of supported vanadium oxide catalysts during methanol oxidation, *Top. Catal.* 11 (2000) 85–100.
- [32] C. Resini, T. Montanari, G. Busca, J.-M. Jehng, I.E. Wachs, Comparison of alcohol and alkane oxidative dehydrogenation reactions over supported vanadium oxide catalysts: in situ infrared, Raman and UV-vis spectroscopic studies of surface alkoxy intermediates and of their surface chemistry, *Catal. Today* 99 (2005) 105–114.
- [33] D.W. Kwon, D.H. Kim, S. Lee, J. Kim, H.P. Ha, A dual catalytic strategy by the nature of the functionalization effect as well as active species on vanadium-based catalyst for enhanced low temperature SCR, *Appl. Catal. B* 289 (2021), 120032.
- [34] L. Xu, C. Wang, H. Chang, Q. Wu, T. Zhang, J. Li, New insight into SO_2 poisoning and regeneration of $\text{CeO}_2\text{--WO}_3/\text{TiO}_2$ and $\text{V}_2\text{O}_5\text{--WO}_3/\text{TiO}_2$ catalysts for low-temperature $\text{NH}_3\text{--SCR}$, *Environ. Sci. Technol.* 52 (2018) 7064–7071.
- [35] H. Liu, J. Chen, Y. Wang, R. Yin, W. Yang, G. Wang, W. Si, Y. Peng, J. Li, Interaction mechanism for simultaneous elimination of nitrogen oxides and toluene over the bifunctional $\text{CeO}_2\text{--TiO}_2$ mixed oxide catalyst, *Environ. Sci. Technol.* 56 (2022) 4467–4476.
- [36] X. Liu, Z. Xing, Y. Zhang, Z. Li, X. Wu, S. Tan, X. Yu, Q. Zhu, W. Zhou, Fabrication of 3D flower-like black $\text{N-TiO}_{2-x}\text{@MoS}_2$ for unprecedented-high visible-light-driven photocatalytic performance, *Appl. Catal. B* 201 (2017) 119–127.
- [37] S. Koust, B.N. Reinecke, K.C. Adamsen, I. Beinik, K. Handrup, Z. Li, P.G. Moses, J. Schnadt, J.V. Lauritsen, S. Wendt, Coverage-dependent oxidation and reduction of vanadium supported on anatase $\text{TiO}_2(1\ 0\ 1)$, *J. Catal.* 360 (2018) 118–126.
- [38] S. Li, W. Huang, H. Xu, T. Chen, Y. Ke, Z. Qu, N. Yan, Alkali-induced deactivation mechanism of $\text{V}_2\text{O}_5\text{--WO}_3/\text{TiO}_2$ catalyst during selective catalytic reduction of NO by NH_3 in aluminum hydrate calcining flue gas, *Appl. Catal. B* 270 (2020), 118872.
- [39] R. Yin, J. Chen, J. Mi, H. Liu, T. Yan, L. Shan, J. Lang, J. Li, Breaking the activity-selectivity trade-off for simultaneous catalytic elimination of nitric oxide and chlorobenzene via $\text{FeVO}_4\text{--Fe}_2\text{O}_3$ interfacial charge transfer, *ACS Catal.* 12 (2022) 3797–3806.
- [40] Q. Hong, H. Xu, X. Pang, W. Liu, Z. Liu, W. Huang, Z. Qu, N. Yan, Reverse conversion treatment of gaseous sulfur trioxide using metastable sulfides from sulfur-rich flue gas, *Environ. Sci. Technol.* 56 (2022) 10935–10944.
- [41] L. Jiang, Z. Luo, Y. Li, W. Wang, J. Li, J. Li, Y. Ao, J. He, V.K. Sharma, J. Wang, Morphology- and phase-controlled synthesis of visible-light-activated S-doped TiO_2 with tunable $\text{S}^{4+}/\text{S}^{6+}$ ratio, *Chem. Eng. J.* 402 (2020).
- [42] T. Kane, J. Guerrero-Caballero, A. Löfberg, H_2S chemical looping selective and preferential oxidation to sulfur by bulk V_2O_5 , *Appl. Catal. B* 265 (2020), 118566.
- [43] H. Fu, X. Wang, H. Wu, Y. Yin, J. Chen, Heterogeneous uptake and oxidation of SO_2 on iron oxides, *J. Phys. Chem. C* 111 (2007) 6077–6085.
- [44] M. Qing, S. Su, L. Wang, L. Liu, K. Xu, L. He, X. Jun, S. Hu, Y. Wang, J. Xiang, Getting insight into the oxidation of SO_2 to SO_3 over $\text{V}_2\text{O}_5\text{--WO}_3/\text{TiO}_2$ catalysts: Reaction mechanism and effects of NO and NH_3 , *Chem. Eng. J.* 361 (2019) 1215–1224.
- [45] T. Yamaguchi, T. Jin, K. Tanabe, Structure of acid sites on sulfur-promoted iron oxide, *J. Phys. Chem.* 90 (1986) 3148–3152.
- [46] Y. Lin, Y. Li, Z. Xu, J. Guo, T. Zhu, Carbon consumption and adsorption-regeneration of H_2S on activated carbon for coke oven flue gas purification, *Environ. Sci. Pollut. Res.* 28 (2021) 60557–60568.
- [47] L. Zhang, H. Qu, T. Du, W. Ma, Q. Zhong, H_2O and SO_2 tolerance, activity and reaction mechanism of sulfated Ni–Ce–La composite oxide nanocrystals in $\text{NH}_3\text{--SCR}$, *Chem. Eng. J.* 296 (2016) 122–131.
- [48] C. Liu, H. Wang, Q. Ma, J. Ma, Z. Wang, L. Liang, W. Xu, G. Zhang, X. Zhang, T. Wang, H. He, Efficient conversion of NO to NO_2 on SO_2 -aged MgO under atmospheric conditions, *Environ. Sci. Technol.* 54 (2020) 11848–11856.
- [49] J. Xiong, Y. Li, Y. Lin, T. Zhu, Formation of sulfur trioxide during the SCR of NO with NH_3 over a $\text{V}_2\text{O}_5/\text{TiO}_2$ catalyst, *RSC Adv.* 9 (2019) 38952–38961.
- [50] Y. Li, J. Xiong, Y. Lin, J. Guo, T. Zhu, Distribution of SO_2 oxidation products in the SCR of NO over $\text{V}_2\text{O}_5/\text{TiO}_2$ catalysts at different temperatures, *Ind. Eng. Chem. Res.* 59 (2020) 5177–5185.
- [51] H. He, C.-G. Zhang, J.-L. Xia, A.-A. Peng, Y. Yang, H.-C. Jiang, L. Zheng, C.-Y. Ma, Y.-D. Zhao, Z.-Y. Nie, G.-Z. Qiu, Investigation of elemental sulfur speciation transformation mediated by acidithiobacillus ferrooxidans, *Curr. Microbiol.* 58 (2009) 300–307.
- [52] D. Klein, The influence of organic liquids upon the interaction of hydrogen sulphide and sulphur dioxide, *J. Phys. Chem.* 15 (1911) 1–19.
- [53] C. Li, M. Shen, T. Yu, J. Wang, J. Wang, Y. Zhai, The mechanism of ammonium bisulfate formation and decomposition over V/WTi catalysts for NH_3 -selective catalytic reduction at various temperatures, *Phys. Chem. Chem. Phys.* 19 (2017) 15194–15206.
- [54] M. Waqif, P. Bazin, O. Saur, J.C. Lavalley, G. Blanchard, O. Touret, Study of ceria sulfation, *Appl. Catal. B* 11 (1997) 193–205.
- [55] G.M.E. Shafei, C.A. Philip, Solid acids from persulfated and perchlorated physical mixtures of zirconium and titanium hydroxides, *Adsorpt. Sci. Technol.* 20 (2002) 977–993.
- [56] T. Jin, T. Yamaguchi, K. Tanabe, Mechanism of acidity generation on sulfur-promoted metal oxides, *J. Phys. Chem.* 90 (1986) 4794–4796.
- [57] J.L. Ropero-Vega, A. Aldana-Pérez, R. Gómez, M.E. Niño-Gómez, Sulfated titania [$\text{TiO}_2/\text{SO}_4^{2-}$]: A very active solid acid catalyst for the esterification of free fatty acids with ethanol, *Appl. Catal. A* 379 (2010) 24–29.
- [58] X. Du, J. Xue, X. Wang, Y. Chen, J. Ran, L. Zhang, Oxidation of sulfur dioxide over $\text{V}_2\text{O}_5/\text{TiO}_2$ catalyst with low vanadium loading: a theoretical study, *J. Phys. Chem. C* 122 (2018) 4517–4523.
- [59] C. Sarzanini, G. Sacchero, F. Pinna, M. Signoretto, G. Cerrato, C. Morterra, Amount and nature of sulfates at the surface of sulfate-doped zirconia catalysts, *J. Mater. Chem.* 5 (1995) 353–360.
- [60] M. Guo, B. Mosevitzky Lis, M.E. Ford, I.E. Wachs, The effect of non-redox promoters (AlO_x , PO_x , SiO_x and ZrO_x) and surface sulfates on supported $\text{V}_2\text{O}_5\text{--WO}_3/\text{TiO}_2$ catalysts in selective catalytic reduction of NO with NH_3 , *Appl. Catal. B* 306 (2022).
- [61] S. Xiong, J. Chen, N. Huang, T. Yan, Y. Peng, J. Li, The poisoning mechanism of gaseous HCl on low-temperature SCR catalysts: $\text{MnO}_x\text{--CeO}_2$ as an example, *Appl. Catal. B* 267 (2020), 118668.
- [62] J. Yuan, J. Mi, R. Yin, T. Yan, H. Liu, X. Chen, J. Liu, W. Si, Y. Peng, J. Chen, J. Li, Identification of intrinsic active sites for the selective catalytic reduction of nitric oxide on metal-free carbon catalysts via selective passivation, *ACS Catal.* 12 (2022) 1024–1030.
- [63] F. Mélen, M. Herman, Vibrational bands of $\text{H}_x\text{N}_y\text{O}_z$ molecules, *J. Phys. Chem. Ref. Data* 21 (1992) 831–881.
- [64] H. Wang, Z. Qu, S. Dong, C. Tang, Mechanistic investigation into the effect of sulfuration on the FeW catalysts for the selective catalytic reduction of NO_x with NH_3 , *ACS Appl. Mater. Interfaces* 9 (2017) 7017–7028.